1 Neural basis of opioid-induced respiratory depression and its rescue.

2 Shijia Liu[1,2], Dongil Kim[1], Tae Gyu Oh[3], Gerald Pao[4], Jonghyun Kim[1], Richard D. Palmiter[5], Matthew R. Banghart[2],

3 Kuo-Fen Lee[1,2], Ronald M. Evans[3], Sung Han[1,2,*]

4 [1]Peptide Biology Laboratories, The Salk Institute for Biological Studies, La Jolla, CA 92037, USA.

5 [2]Section of Neurobiology, Division of Biological Sciences, University of California, San Diego, La Jolla, CA

6 92093, USA.

7 [3]Howard Hughes Medical Institute, Gene Expression Laboratories, The Salk Institute for Biological Studies, La

8 Jolla, CA 92037, USA.

9 [4]Molecular and Cellular Biology Laboratories, The Salk Institute for Biological Studies, La Jolla, CA 92037, USA.

10 [5]Howard Hughes Medical Institute, Department of Biochemistry, School of Medicine, University of Washington,

11 Seattle, WA 98195, USA.

12 *Corresponding author: Sung Han, PhD

13 **Author Contributions:** S.H. conceived the idea, designed and constructed respiratory monitoring apparatus, and

14 secured funding. S.H. and S.L. designed the experiments and wrote the manuscript with inputs from other authors.

15 S.L. performed most of the experiments. D.K. and J.K. prepared the sample for RiboTag RNA sequencing. T.G.O.

16 analyzed the data from RiboTag RNA sequencing. G.M.P. performed the CCM analysis. R.D.P. provided the

17 Oprm1^{Cre} mouse line. M.R.B. provided the hMOR virus. K.F.L. and R.M.E. provided experimental resources.

18 Acknowledgments

23 **Competing Interest Statement:** The authors have declared no conflict of interest.

24

25

26

27

Abstract

Opioid-induced respiratory depression (OIRD) causes death following an opioid overdose, yet the neurobiological mechanisms of this process are not well understood. Here, we show that neurons within the lateral parabrachial nucleus that express the μ-opioid receptor (PBL^{Oprm1} neurons) are involved in OIRD pathogenesis. PBL^{Oprm1} neuronal activity is tightly correlated with respiratory rate, and this correlation is abolished following morphine injection. Chemogenetic inactivation of PBL^{Oprm1} neurons mimics OIRD in mice, whereas their chemogenetic activation following morphine injection rescues respiratory rhythms to baseline levels. We identified several excitatory G-protein coupled receptors expressed by PBL^{Oprm1} neurons and show that agonists for these receptors restore breathing rates in mice experiencing OIRD. Thus, PBL^{Oprm1} neurons are critical for OIRD pathogenesis, providing a promising therapeutic target for treating OIRD in patients.

Introduction

The misuse of prescription and recreational opioids has taken nearly 4.5 million lives between 1999 and 2018 in the United States alone (1). The direct cause of death from opioid overdose is opioid-induced respiratory depression (OIRD) (2, 3). Currently, the only available antidote capable of reversing OIRD is naloxone, a nonselective opioid receptor antagonist. However, naloxone is associated with several disadvantages, namely the reappearance of OIRD due to its short half-life, the inability to reverse high-affinity opioid drugs (e.g., carfentanil and buprenorphine) due to its low binding affinity, and the potential to induce a catecholamine surge at high doses, which can cause cardiopulmonary arrest (4-6). Alternative non-opioid interventions include respiratory stimulants that act on the brainstem respiratory network (e.g., ampakines) or oxygen-sensing cells within the carotid bodies (e.g., K$^+$-channel blockers) (5). However, none of these alternatives are as effective as naloxone, and the safety of these interventions has not been well documented. Therefore, novel treatment strategies are needed, and more effective countermeasures can only be developed with a mechanistic understanding of OIRD pathogenesis.

Neural substrates that contribute to OIRD pathogenesis should satisfy two criteria. They should localize to the breathing control network and express the μ-opioid receptor (MOR, encoded by the *Oprm1* gene), which has been demonstrated as the primary mediator of both the analgesic and respiratory effects of opioids (7, 8). Two candidate structures satisfy these criteria, namely the pre-Bötzinger complex (preBötC) and the parabrachial complex (9-17). The former lies in the ventrolateral medulla and is the primary generator of the respiratory rhythm (18-20). The parabrachial complex, including the lateral parabrachial, medial parabrachial, and Kölliker-Fuse (KF) nuclei, is located in the dorsolateral pons and modulates breathing (21-23), in response to homeostatic disturbances

2

58   such as CO_2/O_2 imbalance and noxious stimuli (24-28). Recent studies have suggested the involvement of these

59   two brain regions on OIRD pathogenesis by using either pharmacological or genetic approaches. Direct infusion of

60   opioid agonists or antagonists into these brain areas induces or attenuates OIRD (9, 12, 29, 30). Region-specific

61   genetic deletion of the *Oprm1* genes by viral delivery of Cre-recombinase into these areas of the *Oprm1*-floxed

62   mice also attenuates OIRD (13, 14). However, the pharmacological approach lacks considerable specificity

63   primarily due to the local diffusion of drugs and the difficulty of reproducible targeting, whereas the genetic deletion

64   approach is often incomplete and prevents the possibility to directly control the neuronal activity in a spatially and

65   temporally precise manner. As a result, discrepancies arise over the critical site of action responsible for OIRD (13,

66   14, 16, 17). To expand the scope of current research, our paper utilizes contemporary cell-type-specific approaches

67   to characterize the role of a defined neuronal population in morphine-induced respiratory depression. This will

68   allow us to better understand its cellular and physiological mechanisms and make inroads in developing therapeutic

69   strategies.

70   Here we report that a genetically defined population of neurons that encodes the *Oprm1* gene in the lateral

71   parabrachial nucleus (PBL*Oprm1* neurons) is an important regulator of respiratory rhythm. Inhibition of these neurons

72   by opioids leads to respiratory depression. Furthermore, we show that both chemogenetic activation of these neurons

73   and pharmacological activation of endogenous G-protein coupled receptors (GPCRs) expressed specifically in these

74   neurons completely rescues OIRD in mice.

75

Results

76

77   To examine the contributions of global MOR signaling to OIRD, we generated an *Oprm1* reporter mouse
78 line in which the endogenous *Oprm1* gene was knocked out by inserting a Cre:GFP cassette upstream of the start
79 codon ($Oprm1^{Cre}$) (Figure 1B and Supplementary Figure 1A for validation), and measured the effects of systemic
80 morphine injection on breathing rhythms via whole-body plethysmography (Figure 1A). After receiving a morphine
81 injection, wild-type mice exhibited a significantly lower respiratory rate ($46.5 \pm 3.1\%$ of the pre-morphine baseline
82 (data are represented as mean $\pm$ SEM throughout the paper)). In contrast, mice lacking one or both functional copies
83 of the *Oprm1* gene ($Oprm1^{Cre/+}$ and $Oprm1^{Cre/Cre}$) exhibited more moderate reductions in respiratory rate ($63.2 \pm$
84 2.8% and $91.2 \pm 2.8\%$ of the pre-morphine baseline, respectively) (Figure 1C, D). *Oprm1*, therefore, plays a vital
85 role in OIRD.

86   We then used pharmacological and genetic tools to manipulate opioid signaling specifically in the PBL.
87 First, wild-type mice received a systemic injection of morphine followed by an infusion of naloxone directly into
88 the PBL (Figure 1E). To facilitate stereotaxic naloxone delivery, we lightly anesthetized mice with 1-1.5%
89 isoflurane and monitored their breathing using a piezoelectric sensor that detects chest movements (31). After
90 systemic injection of morphine, the breathing rate dramatically decreased from 121.0 ± 3.4 bpm to 89.1 ± 3.5 bpm,
91 and subsequent stereotaxic injection of naloxone into the PBL recovered the breathing rate back to pre-morphine
92 baseline (120.8 ± 3.7 bpm) (Figure 1F, G). We then explored whether the expression of the *Oprm1* gene in the PBL
93 is necessary and sufficient for OIRD. To assess necessity, we conditionally knocked out the *Oprm1* gene using
94 stereotaxic delivery of a recombinant adeno-associated virus (AAV) expressing Cre recombinase into the PBL
95 of the $Oprm1^{fl/fl}$ mice, in which the *Oprm1* gene is flanked by loxP sites (Figure 1H). Compared to mice receiving
96 GFP-expressing control virus, PBL-specific knockout of the *Oprm1* gene attenuated OIRD following systemic
97 injection of morphine, as measured by whole-body plethysmography (breathing rate changes in GFP group: -136.6
98 ± 21.1 bpm; Cre group: -76.4 ± 11.6 bpm) (Figure 1I and Supplementary Figure 2A-C). To test sufficiency, we
99 reintroduced the wild-type *Oprm1* gene into the PBL^{Oprm1} neurons of Cre-expressing *Oprm1*-null mice. This was
100 achieved by injecting an AAV expressing Cre-dependent human MOR (AAV-hSyn-DIO-mCherry-T2A-FLAG-
101 hMOR) (Figure 1J) into the PBL of $Oprm1^{Cre/Cre}$ mice. Selective expression of hMOR in the PBL restored the OIRD
102 phenotype (hMOR group, post-saline: 359.0 ± 5.1 bpm; post-morphine: 299.0 ± 3.6 bpm) compared to the
103 control group (Figure 1K and Supplementary Figure 2D). Note that the breathing rate measured by the piezoelectric
104 sensor under anesthesia (Figure 1G) is ~3-fold lower than that measured in a plethysmography chamber (Figure
105 1K). Together, these data strongly support the conclusion that the *Oprm1* gene expression in the PBL mediates
106 OIRD in mice.

107   We then focused on PBL^{Oprm1} neurons and explored their relationship with OIRD. PBL^{Oprm1} neurons are

108   mostly glutamatergic and express higher levels of the *Oprm1* gene than the adjacent KF nucleus, which provides

109   post-inspiratory drive (13, 23, 31, 32) (Supplementary Figure 1B-C). We devised an experimental platform to

110   simultaneously measure PBL^{Oprm1} neuronal activity and respiration in awake, freely moving mice using fiber-

111   photometry calcium imaging *in vivo* with a thermistor implanted into the nasal cavity (Figure 2A). The thermistor-

112   based respiration monitoring device detects the temperature change between inhaled and exhaled air and converts

113   breath-to-breath fluctuations in resistance into voltage signals (33). We stereotaxically injected an AAV expressing

114   Cre-dependent jGCaMP7s (AAV-DIO-jGCaMP7s) into the PBL, then implanted an optic fiber into the PBL of

115   *Oprm1$^{Cre/+}$* mice and a respiration sensor in the nasal cavity (Figure 2B). PBL^{Oprm1} activity and breathing rate

116   exhibited a tight positive correlation (Figure 2C-D, H). Moreover, morphine administration substantially decreased

117   the breathing rate ($46.5 \pm 3.9\%$ of the pre-morphine baseline) (Figure 2H, J, L, and N) despite the potent effect

118   morphine has on locomotor sensitization (Supplementary Figure 3), which one would expect to elevate the breathing

119   rate. Besides, morphine decreased calcium activity (Figure 2H, J, O, and Q), as well as eliminated any spontaneous

120   fluctuations in both breathing and calcium signals (Figure 2N, Q). In contrast, saline injection largely preserved the

121   original patterns of the signals (Figure 2D, 2F, 2L-M, and 2O-P). Using convergent cross-mapping (CCM) (34), a

122   statistical algorithm that makes predictions from independent time-series data, we predicted changes in respiratory

123   rate using the calcium signal as input ($76.2 \pm 8.1\%$, pre-morphine predictability) (Supplementary Figure 4).

124   Interestingly, systemic morphine administration not only reduced the correlation coefficient (Figure 2I, K) but also

125   completely abolished the predictive relationship between respiratory rate and the calcium signal ($12.5 \pm 20.2\%$,

126   post-morphine predictability) (Supplementary Figure 4C-D). Conversely, the saline injection did not alter the

127   correlation between these signals (Fig 2E, G, and Supplementary Figure 4A-B). These results indicate that PBL^{Oprm1}

128   neurons are critically involved in modulating respiratory rate and that morphine suppresses both the PBL^{Oprm1}

129   neuronal activity and its coupling with the breathing rate.

130   To further investigate PBL^{Oprm1} neurons' role in breathing regulation, we specifically manipulated their

131   activity using chemogenetic tools, namely Designer Receptor Exclusively Activated by Designer Drugs

132   (DREADD) (35). If PBL^{Oprm1} neurons directly regulate breathing, inhibiting their activity via a $G_{i/o}$-coupled

133   DREADD should recapitulate the OIRD phenotype. Furthermore, this should also happen in *Oprm1* knockout mice,

134   which failed to display OIRD when given systemic morphine (Figure 1C-D). We expressed a κ-opioid receptor-

135   derived DREADD (KORD) (36) Cre-dependently and bilaterally in PBL^{Oprm1} neurons of *Oprm1$^{Cre/Cre}$* mice (Figure

136   3A). Systemic injection of its synthetic ligand, salvinorin B (SALB), decreased the respiratory rate (317.8 ± 3.6

137   bpm) compared to the DMSO-injected control group (342.4 ± 4.1 bpm) (Figure 3B and Supplementary Figure 5A-

138   B). We did not observe significant breathing amplitude changes upon SALB injection in either control or KORD-

139   expressing animals (Supplementary Figure 5B-C).

140   We next asked whether artificial activation of PBL^{Oprm1} neurons could prevent OIRD in mice. We expressed

141   hM3Dq, a metabotropic acetylcholine receptor-derived excitatory DREADD, in PBL^{Oprm1} neurons via bilateral

142   injection of an AAV encoding Cre-dependent hM3Dq into $Oprm1^{Cre/+}$ mice (Figure 3C). Additionally, we implanted

143   a micro-thermistor sensor into the nasal cavity to monitor respiratory rhythm in awake, freely moving mice over

144   the course of OIRD (Supplementary Figure 5D). Upon systemic morphine injection, the respiratory rate decreased

145   significantly within 10 min (from 332.0 ± 25.6 bpm to 124.6 ± 9.1 bpm) (Figure 3D-E). We then systemically

146   injected the hM3Dq agonist, clozapine-N-oxide (CNO), into the same animal to activate PBL^{Oprm1} neurons. CNO

147   injection increased the breathing rate in hM3Dq-expressing animals (268.0 ± 13.5 bpm) to a level comparable to

148   controls that did not receive morphine (275.7 ± 24.9 bpm). Nevertheless, CNO did not rescue breathing rates in

149   eYFP-expressing control animals (120.0 ± 4.3 bpm) (Figure 3D-F and Supplementary Figure 5E). A complete

150   rescue was also observed in minute volume (Supplementary Figure 5F, G). These data show that activation of

151   PBL^{Oprm1} neurons is sufficient to restore normal breathing rhythms in mice displaying OIRD.

152   Having determined that chemogenetic activation of PBL^{Oprm1} neurons could effectively prevent OIRD, we

153   sought to identify endogenous signaling pathways that could be used to activate PBL^{Oprm1} neurons. To identify the

154   active transcriptome enriched in PBL^{Oprm1} neurons, we sequenced ribosome-associated mRNAs from the PBL of

155    $Oprm1^{Cre}$::RiboTag mice, which express hemagglutinin (HA)-tagged ribosomal protein Rpl22 in $Oprm1^{+}$ neurons

156   (Figure 4A-B) (37). We identified 69 mRNAs upregulated over three folds in PBL^{Oprm1} neurons than non-$Oprm1$

157   neurons in the PBL (Figure 4C). $Oprm1$, as well as other major parabrachial markers ($Tac1, Foxp2$, and $Adcyap1$)

158   were enriched, but $Calca$ and $Pdyn$, markers for the external lateral and dorsal lateral parabrachial nucleus, were

159   not (38, 39). Notably, the PBL^{Oprm1} active transcriptome revealed several GPCRs expressed at high levels in these

160   neurons, which we subsequently investigated as potential pharmacological targets to rescue OIRD.

161   We selected five excitatory GPCRs for pharmacological manipulation and confirmed that they were

162   expressed in PBL^{Oprm1} neurons by RNA in $situ$ hybridization (Supplementary Figure 6A-B). These GPCRs were 5-

163   hydroxytryptamine receptor 2A ($Htr2a$), cholecystokinin A receptor ($Cckar$), tachykinin receptor 1 ($Tacr1$),

164   tachykinin receptor 3 ($Tacr3$), and dopamine receptor D5 ($Drd5$). We systemically injected their agonists (TCB-2,

165   CCK8S, Substance P, Senktide, and SKF83959, respectively) into the PBL of anesthetized mice after inducing

166   OIRD (breathing rate before morphine: 115.4 ± 1.6 bpm, after morphine: 77.9 ± 2.3 bpm; Figure 4D-E and

167   Supplementary Table 1). Three of the five agonists tested (TCB-2, CCK8S, and Substance P) increased the

168   respiratory rate (98.1 ± 7.9, 117.1 ± 6.4, 100.8 ± 4.6 bpm; Figure 4F and Supplementary Figure 6C-E). Notably,

169   these same drugs have been shown to modulate respiratory rhythm in different contexts by activating other

170   respiratory centers, and some have been associated with an anti-morphine effect (40-42). Our findings suggest that

171   activating PBL^{Oprm1} neurons through endogenous signaling pathways may effectively treat OIRD in patients.

172   **Discussion**

173   We have identified a population of neurons in the pontine respiratory group, the PBL^{Oprm1} neurons, as

174   critical mediators of morphine-induced respiratory depression and candidates for its rescue in intact mice. Genetic

175   deletion of *Oprm1* from the PBL attenuated OIRD, while reintroducing human MOR into the PBL^{Oprm1} neurons

176   restored OIRD. By combining cell-type-specific tools with breathing monitoring in awake behaving mice, we have

177   demonstrated that PBL^{Oprm1} neurons are regulators of the breathing rhythm and pattern. Systemic morphine

178   administration dramatically abolishes the activity of these neurons and weakens their control on breathing.

179   Furthermore, chemogenetic inhibition of PBL^{Oprm1} neurons mimics OIRD, and prolonged optogenetic inhibition of

180   PBL^{Oprm1} neurons induces apnea (observations from our group (43)), which precedes cardiorespiratory collapse

181   prior to overdose-induced death. By contrast, artificial activation of PBL^{Oprm1} neurons, either chemogenetically or

182   pharmacologically, successfully restores breathing in mice experiencing OIRD (Supplementary Figure 7).

183   **Investigating OIRD with cell-type-specific approaches.**

184   Recent studies have demonstrated the involvement of both pontine and medullary respiratory groups in

185   OIRD (13, 14) without reaching a consensus on the key players. We think this is mostly due to the lack of specificity

186   from the pharmacological and genetic deletion approaches and the intricacies of physiological preparations, both of

187   which hampers reproducibility. In comparison, we exploited the *Oprm1*^{Cre} mouse line which provides access to a

188   restricted neuronal population, and obtained multi-faceted evidence supporting the role of the parabrachial nucleus

189   in OIRD. In our view, OIRD is a synergistic outcome from impairment of the interconnected pontomedullary

190   breathing network that widely expresses MOR both pre- and post-synaptically (10, 11, 30, 44, 45). For example,

191   parabrachial neurons send tonic excitatory inputs to the preBötC (39, 43, 46, 47), and both of these areas express

192   MOR (18, 48).

193   One challenge of elucidating the OIRD mechanism is how to access a group of neurons while

194   simultaneously record breathing over the course of OIRD. Traditional respiratory monitoring approaches in rodents,

195   such as *in situ* or *in vivo* anesthetized preparations and plethysmography chambers, are more challenging to achieve

196   this goal. Therefore, we utilized the implantable temperature sensor to monitor breathing in awake, unrestrained,

197   behaving mice with unprecedented freedom to access the brain due to its open configuration. With this approach,

198   we implemented chemogenetics and *in vivo* calcium imaging while simultaneously monitored breathing rhythms.

199   Similar techniques can be applied to the *Oprm1*-expressing neurons in the preBötC, KF, the postinspiratory complex

200   (49), and other respiratory centers to resolve the long-standing debate on their contributions in OIRD (16, 17).

201   **PBL^{Oprm1} neurons' role in breathing regulation and OIRD.**

7

202   The parabrachial complex has long been reported to modulate respiration and sometimes exert opposing

203   effects depending on the location of artificial manipulation (21-23). Stimulation of the PBL results in tachypnea,

204   whereas stimulation of the KF elicits prolonged post-inspiration and bradypnea (13, 31, 32). Consistent with these

205   previous reports, our monitoring and manipulation data suggest that PBL^{Oprm1} neurons have the most substantial

206   effect on the breathing rate (23). In addition to breathing, the PBL also regulates various homeostatic functions (39)

207   and incorporates the alarm center, which senses deviations from the homeostasis and relays aversive signals to

208   higher-order brain structures (38, 50). At the same time, by sending tonic excitatory outputs to medulla respiratory

209   centers (39, 43, 46), the parabrachial neurons can increase breathing rhythm under conditions that immediately

210   require more oxygen due to metabolic needs, such as hypoxia (27) and hypercapnia (26), in particular, hypercapnic

211   arousal during sleep (24, 28, 51); or non-metabolic behavioral demands, such as escaping from a threat (25). As a

212   representative glutamatergic population in the PBL (Supplementary Figure 1), *Oprm1*-positive neurons are likely

213   to participate in similar physiological processes. Our data demonstrated that an overdose of morphine shuts down

214   PBL^{Oprm1} neurons' activity, preventing them from responding to conditions that decrease respiratory rhythm. These

215   conditions may include hypoxia, hypercapnia, anesthesia, or sedative drug treatment. Indeed, the incidence of OIRD

216   is dramatically increased when opioids are used together with sedatives and anesthetics (52), and the failure to

217   increase respiratory behavior in response to hypercapnic gas is one characteristic of OIRD (3). On the contrary, a

218   mild inhibition of PBL^{Oprm1} neurons may explain many of the behavioral effects of lower doses of endogenous or

219   exogenous opioids, such as slowed breathing, calmness, and reward (43). The current study used morphine as a

220   starting point to induce OIRD, and further investigation is required to determine the involvement of PBL^{Oprm1}

221   neurons under the challenge of other types of sedative agents.

222   **A proof of principle of rescuing OIRD by activating a pontine population.**

223   PBL^{Oprm1} neurons are among the key nodes most vulnerable to opioid action, and their activation is

224   sufficient to restore the breathing rate and tidal volume following morphine administration. This activation can be

225   achieved by exploiting both artificial and, more importantly, endogenous signaling pathways. Besides, manipulating

226   PBL^{Oprm1} neurons located in the dorsolateral pons is associated with lower risk than the respiratory

227   rhythm generators within the deep medulla. We have provided a proof of concept of rescuing OIRD by activating

228   endogenous $G_{q/s}$-coupled GPCRs expressed in PBL^{Oprm1} neurons (Supplementary Figure 7). In principle, cell-type-

229   specific manipulation can also be achieved through the collective activation of multiple GPCRs.

230   Our transcriptomic profiling data suggested that other neuromodulators, such as serotonin, cholecystokinin,

231   and tachykinin, may also involve in respiratory regulation with potential interplay with the opioid system (40-42).

232   The same receptor that we identified, Htr2a, has recently been confirmed to express in the PBL and mediate

233   hypercapnia-induced arousal by integrating serotonergic inputs from the dorsal raphe (51). It would be interesting

234   to identify other neuromodulatory circuits that may be involved in the regulation of OIRD. Similar transcriptomic

235   profiling strategies can also be applied to the broader breathing control network to exploit the therapeutic potential

236   of GPCRs in reversing OIRD.

237

238

239

240

241

242

243

244

245

246

247

248

249

250

251

252

253

254

255

256

257

258

259

260

261

262

263

264

265

References

266

267   1.   H. Hedegaard, A. M. Miniño, M. Warner, Drug overdose deaths in the United States, 1999-2018. *NCHS*
268   *data brief* **356** (2020).

269   2.   K. T. Pattinson, Opioids and the control of respiration. *Br. J. Anaesth.* **100**, 747-758 (2008).

270   3.   A. Dahan, L. Aarts, T. W. Smith, Incidence, reversal, and prevention of opioid-induced respiratory
271   depression. *Anesthesiology* **112**, 226-238 (2010).

272   4.   P. Skolnick, On the front lines of the opioid epidemic: rescue by naloxone. *European journal of*
273   *pharmacology* **835**, 147-153 (2018).

274   5.   A. Dahan *et al.*, Averting opioid-induced respiratory depression without affecting analgesia. *Anesthesiology*
275   **128**, 1027-1037 (2018).

276   6.   E. W. Boyer, Management of opioid analgesic overdose. *N. Engl. J. Med.* **367**, 146-155 (2012).

277   7.   H. W. Matthes *et al.*, Loss of morphine-induced analgesia, reward effect and withdrawal symptoms in mice
278   lacking the μ-opioid-receptor gene. *Nature* **383**, 819 (1996).

279   8.   A. Dahan *et al.*, Anesthetic Potency and Influence of Morphine and Sevoflurane on Respiration in μ-Opioid
280   Receptor Knockout Mice. *Anesthesiology* **94**, 824-832 (2001).

281   9.   J. R. Miller *et al.*, A Subregion of the Parabrachial Nucleus Partially Mediates Respiratory Rate Depression
282   from Intravenous Remifentanil in Young and Adult Rabbits. *Anesthesiology* **127**, 502-514 (2017).

283   10.   E. Cinelli, F. Bongianni, T. Pantaleo, D. Mutolo, Activation of μ-opioid receptors differentially affects the
284   preBötzinger Complex and neighbouring regions of the respiratory network in the adult rabbit. *Respir.*
285   *Physiol. Neurobiol.* **280**, 103482 (2020).

286   11.   A. D. Wei, J.-M. Ramirez, Presynaptic mechanisms and KCNQ potassium channels modulate opioid
287   depression of respiratory drive. *Front. Physiol.* **10**, 1407 (2019).

288   12.   I. Prkic *et al.*, Pontine mu-opioid receptors mediate bradypnea caused by intravenous remifentanil infusions
289   at clinically relevant concentrations in dogs. *J. Neurophysiol.* **108**, 2430-2441 (2012).

290   13.   A. G. Varga, B. T. Reid, B. L. Kieffer, E. S. Levitt, Differential impact of two critical respiratory centres
291   in opioid-induced respiratory depression in awake mice. *The Journal of Physiology* **598**, 189-205 (2020).

292   14.   I. Bachmutsky, X. P. Wei, E. Kish, K. Yackle, Opioids depress breathing through two small brainstem sites.
293   *Elife* **9**, e52694 (2020).

294   15.   G. Montandon *et al.*, PreBotzinger complex neurokinin-1 receptor-expressing neurons mediate opioid-
295   induced respiratory depression. *J. Neurosci.* **31**, 1292-1301 (2011).

296   16.   G. Montandon, R. Horner, CrossTalk proposal: The preBotzinger complex is essential for the respiratory
297   depression following systemic administration of opioid analgesics. *J. Physiol.* **592**, 1159-1162 (2014).

298 17. P. M. Lalley, P. M. Pilowsky, H. V. Forster, E. J. Zuperku, CrossTalk opposing view: The pre-Botzinger
299   complex is not essential for respiratory depression following systemic administration of opioid analgesics.
300   *J. Physiol.* **592**, 1163-1166 (2014).
301 18. C. A. Del Negro, G. D. Funk, J. L. Feldman, Breathing matters. *Nat. Rev. Neurosci.* **19**, 351-367 (2018).
302 19. J. C. Smith, H. H. Ellenberger, K. Ballanyi, D. W. Richter, J. L. Feldman, Pre-Bötzinger complex: a
303   brainstem region that may generate respiratory rhythm in mammals. *Science* **254**, 726-729 (1991).
304 20. Y. Cui *et al.*, Defining preBotzinger Complex Rhythm- and Pattern-Generating Neural Microcircuits In
305   Vivo. *Neuron* **91**, 602-614 (2016).
306 21. N. L. Chamberlin, C. B. Saper, Topographic organization of respiratory responses to glutamate
307   microstimulation of the parabrachial nucleus in the rat. *J. Neurosci.* **14**, 6500-6510 (1994).
308 22. M. Dutschmann, T. E. Dick, Pontine mechanisms of respiratory control. *Compr Physiol* **2**, 2443-2469
309   (2012).
310 23. A. A. Navarrete-Opazo *et al.*, Endogenous glutamatergic inputs to the Parabrachial Nucleus/Kölliker-Fuse
311   Complex determine respiratory rate. *Respir. Physiol. Neurobiol.* **277**, 103401 (2020).
312 24. S. Kaur *et al.*, A Genetically Defined Circuit for Arousal from Sleep during Hypercapnia. *Neuron* **96**, 1153-
313   1167 e1155 (2017).
314 25. M. Jiang, G. F. Alheid, T. Calandriello, D. R. McCrimmon, Parabrachial-lateral pontine neurons link
315   nociception and breathing. *Respir. Physiol. Neurobiol.* **143**, 215-233 (2004).
316 26. G. Song, C. S. Poon, Lateral parabrachial nucleus mediates shortening of expiration and increase of
317   inspiratory drive during hypercapnia. *Respir. Physiol. Neurobiol.* **165**, 9-12 (2009).
318 27. G. Song, C. S. Poon, Lateral parabrachial nucleus mediates shortening of expiration during hypoxia. *Respir.*
319   *Physiol. Neurobiol.* **165**, 1-8 (2009).
320 28. S. Kaur *et al.*, Glutamatergic signaling from the parabrachial nucleus plays a critical role in hypercapnic
321   arousal. *J. Neurosci.* **33**, 7627-7640 (2013).
322 29. S. E. Saunders, E. S. Levitt, Kölliker-Fuse/Parabrachial complex mu opioid receptors contribute to fentanyl-
323   induced apnea and respiratory rate depression. *Respir. Physiol. Neurobiol.* **275**, 103388 (2020).
324 30. P. M. Lalley, Opiate slowing of feline respiratory rhythm and effects on putative medullary phase-
325   regulating neurons. *Am. J. Physiol. Regul. Integr. Comp. Physiol.* **290**, R1387-1396 (2006).
326 31. E. S. Levitt, A. P. Abdala, J. F. Paton, J. M. Bissonnette, J. T. Williams, mu opioid receptor activation
327   hyperpolarizes respiratory-controlling Kolliker-Fuse neurons and suppresses post-inspiratory drive. *J.*
328   *Physiol.* **593**, 4453-4469 (2015).

329   32.   M. Dutschmann, H. Herbert, The Kolliker-Fuse nucleus gates the postinspiratory phase of the respiratory
330   cycle to control inspiratory off-switch and upper airway resistance in rat. *Eur. J. Neurosci.* **24**, 1071-1084
331   (2006).

332   33.   S. S. McAfee *et al.*, Minimally invasive highly precise monitoring of respiratory rhythm in the mouse using
333   an epithelial temperature probe. *J. Neurosci. Methods* **263**, 89-94 (2016).

334   34.   G. Sugihara *et al.*, Detecting Causality in Complex Ecosystems. *Science* **338**, 496-500 (2012).

335   35.   B. L. Roth, DREADDs for Neuroscientists. *Neuron* **89**, 683-694 (2016).

336   36.   E. Vardy *et al.*, A new DREADD facilitates the multiplexed chemogenetic interrogation of behavior.
337   *Neuron* **86**, 936-946 (2015).

338   37.   E. Sanz, J. C. Bean, D. P. Carey, A. Quintana, G. S. McKnight, RiboTag: Ribosomal Tagging Strategy to
339   Analyze Cell-Type-Specific mRNA Expression In Vivo. *Curr. Protoc. Neurosci.* **88**, e77 (2019).

340   38.   R. D. Palmiter, The Parabrachial Nucleus: CGRP Neurons Function as a General Alarm. *Trends Neurosci.*
341   **41**, 280-293 (2018).

342   39.   D. Huang, F. S. Grady, L. Peltekian, J. C. Geerling, Efferent Projections of Vglut2, Foxp2 and Pdyn
343   Parabrachial Neurons in Mice. *J. Comp. Neurol.* https://doi.org/10.1002/cne.24975 (2020).

344   40.   M. Niebert *et al.*, Expression and function of serotonin 2A and 2B receptors in the mammalian respiratory
345   network. *PLoS One* **6**, e21395 (2011).

346   41.   H. H. Ellenberger, F. M. Smith, Sulfated cholecystokinin octapeptide in the rat: pontomedullary distribution
347   and modulation of the respiratory pattern. *Can. J. Physiol. Pharmacol.* **77**, 490-504 (1999).

348   42.   J. Hedner, T. Hedner, P. Wessberg, J. Jonason, Interaction of substance P with the respiratory control system
349   in the rat. *Journal of Pharmacology and Experimental Therapeutics* **228**, 196-201 (1984).

350   43.   S. Liu *et al.*, Identification of a novel breathing circuit that controls pain and anxiety. *bioRxiv*
351   https://doi.org/10.1101/2020.01.09.900738 (2020).

352   44.   U. Arvidsson *et al.*, Distribution and targeting of a mu-opioid receptor (MOR1) in brain and spinal cord. *J.*
353   *Neurosci.* **15**, 3328-3341 (1995).

354   45.   M. A. Hurlé, A. Mediavilla, J. Florez, Differential respiratory patterns induced by opioids applied to the
355   ventral medullary and dorsal pontine surfaces of cats. *Neuropharmacology* **24**, 597-606 (1985).

356   46.   S. Yokota, S. Kaur, V. G. VanderHorst, C. B. Saper, N. L. Chamberlin, Respiratory-related outputs of
357   glutamatergic, hypercapnia-responsive parabrachial neurons in mice. *J. Comp. Neurol.* **523**, 907-920
358   (2015).

359   47.   C. E. Fulwiler, C. B. Saper, Subnuclear organization of the efferent connections of the parabrachial nucleus
360   in the rat. *Brain Res. Rev.* **7**, 229-259 (1984).

361   48.   E. Erbs *et al.*, A mu-delta opioid receptor brain atlas reveals neuronal co-occurrence in subcortical
362   networks. *Brain Struct. Funct.* **220**, 677-702 (2015).

363   49.   T. M. Anderson *et al.*, A novel excitatory network for the control of breathing. *Nature* **536**, 76-80 (2016).

364   50.   K. Tokita, T. Inoue, J. D. Boughter, Afferent connections of the parabrachial nucleus in C57BL/6J mice.
365   *Neuroscience* **161**, 475-488 (2009).

366   51.   S. Kaur *et al.*, Role of serotonergic dorsal raphe neurons in hypercapnia-induced arousals. *Nature*
367   *Communications* **11**, 1-15 (2020).

368   52.   K. Gupta *et al.*, Risk factors for opioid-induced respiratory depression and failure to rescue: a review. *Curr.*
369   *Opin. Anaesthesiol.* **31**, 110-119 (2018).

370   53.   G. Sugihara, R. M. May, Nonlinear forecasting as a way of distinguishing chaos from measurement error
371   in time series. *Nature* **344**, 734-741 (1990).

372   54.   E. R. Deyle, G. Sugihara, Generalized theorems for nonlinear state space reconstruction. *PLoS One* **6**,
373   e18295 (2011).

374   55.   H. Whitney, The imbedding of manifolds in families of analytic manifolds. *Annals of Mathematics*, 865-
375   878 (1936).

376   56.   A. M. Fraser, H. L. Swinney, Independent coordinates for strange attractors from mutual information. *Phys*
377   *Rev A Gen Phys* **33**, 1134-1140 (1986).

378   57.   E. Sanz *et al.*, Cell-type-specific isolation of ribosome-associated mRNA from complex tissues.
379   *Proceedings of the National Academy of Sciences* **106**, 13939-13944 (2009).

380   58.   A. Dobin *et al.*, STAR: ultrafast universal RNA-seq aligner. *Bioinformatics* **29**, 15-21 (2013).

381   59.   B. Li, C. N. Dewey, RSEM: accurate transcript quantification from RNA-Seq data with or without a
382   reference genome. *BMC Bioinformatics* **12**, 323 (2011).

383

384
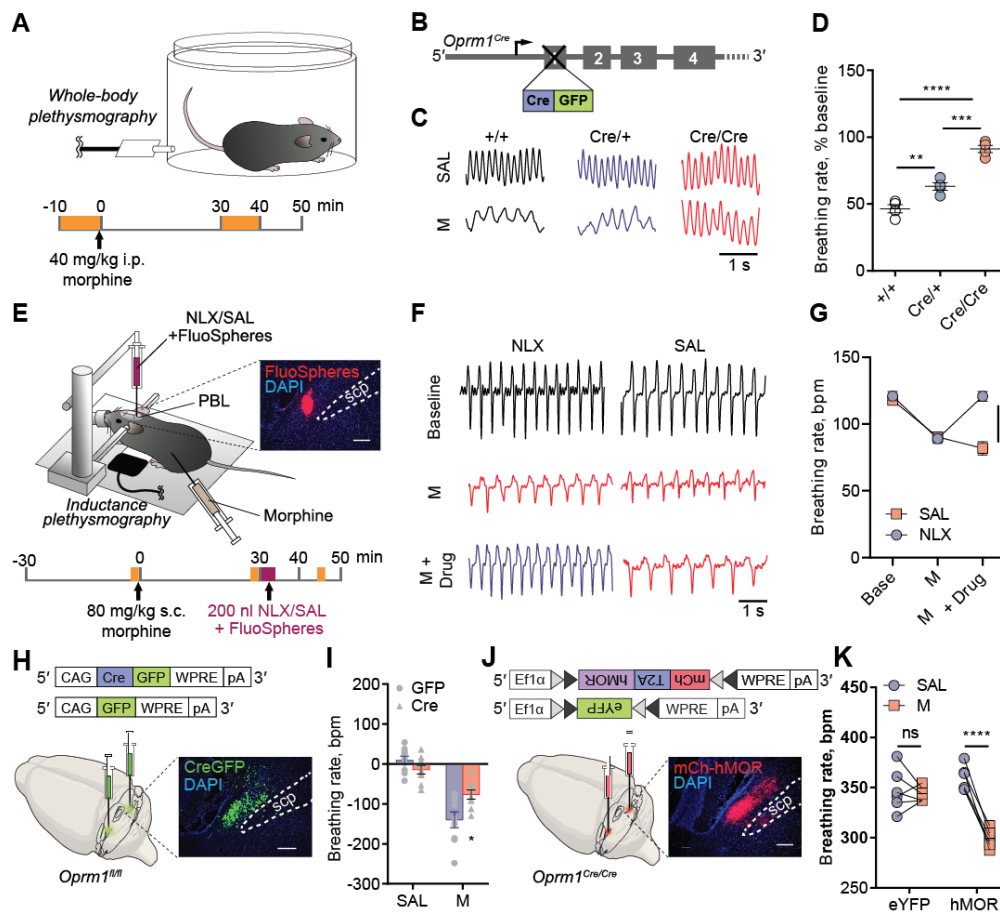
Figure 1. MOR signaling in the PBL mediates morphine-induced respiratory depression. (**A**) Schematics of breathing monitoring in awake mice with whole-body plethysmography before and after systemic morphine injection (refer to **C**, **D**, **I**, **K**). (**B-D**) *Oprm1$^{+/+}$*, *Oprm1$^{Cre/+}$*, and *Oprm1$^{Cre/Cre}$* mice (**B**) displayed different breathing patterns (**C**) and rate changes (**D**) in response to systemic morphine injection. (**E**) Schematics of breathing monitoring in anesthetized mice with inductance plethysmography, during systemic morphine injection and PBL-specific blockade of MOR signaling. Onset, histology of the co-injected FluoSpheres in the PBL. Scp, superior cerebellar peduncle. (**F**) Representative plethysmographs from naloxone (NLX) and saline (SAL) injected groups before morphine, after morphine, and after drug injections into the PBL. (**G**) Injecting naloxone (n = 5), but not saline (n = 5) into the PBL rescued morphine-induced respiratory depression. (**H**) Schematics of PBL-specific knockout of the *Oprm1* gene by stereotaxically injecting AAV-Cre-GFP into the PBL of the *Oprm1$^{fl/fl}$* mice. (**I**) PBL-specific *Oprm1* knockout (n = 9) significantly attenuated OIRD compared to the GFP injected control group (n = 9) after systemic morphine injection. (**J**) Schematics of PBL-specific rescue of the *Oprm1* gene in *Oprm1*-null background by stereotaxically injecting AAV-DIO-hMOR into the PBL of the *Oprm1$^{Cre/Cre}$* mice. (**K**) Mice with PBL-specific rescue of *Oprm1* (n = 6) displayed OIRD phenotype, whereas eYFP injected control group (n = 6) remained insensitive after systemic morphine injection. Data are presented as mean ± SEM. Statistical tests, One-way ANOVA with Tukey's multiple comparison post-hoc test (**D**) or Two-way ANOVA with Bonferroni's multiple comparison post-hoc test (**G, I, K**). *, $p < 0.05$; **, $p < 0.01$; ***, $p < 0.001$; ****, $p < 0.0001$. Scale bar, 1s (**C, F**) or 200 μm (**E, H, J**).

14
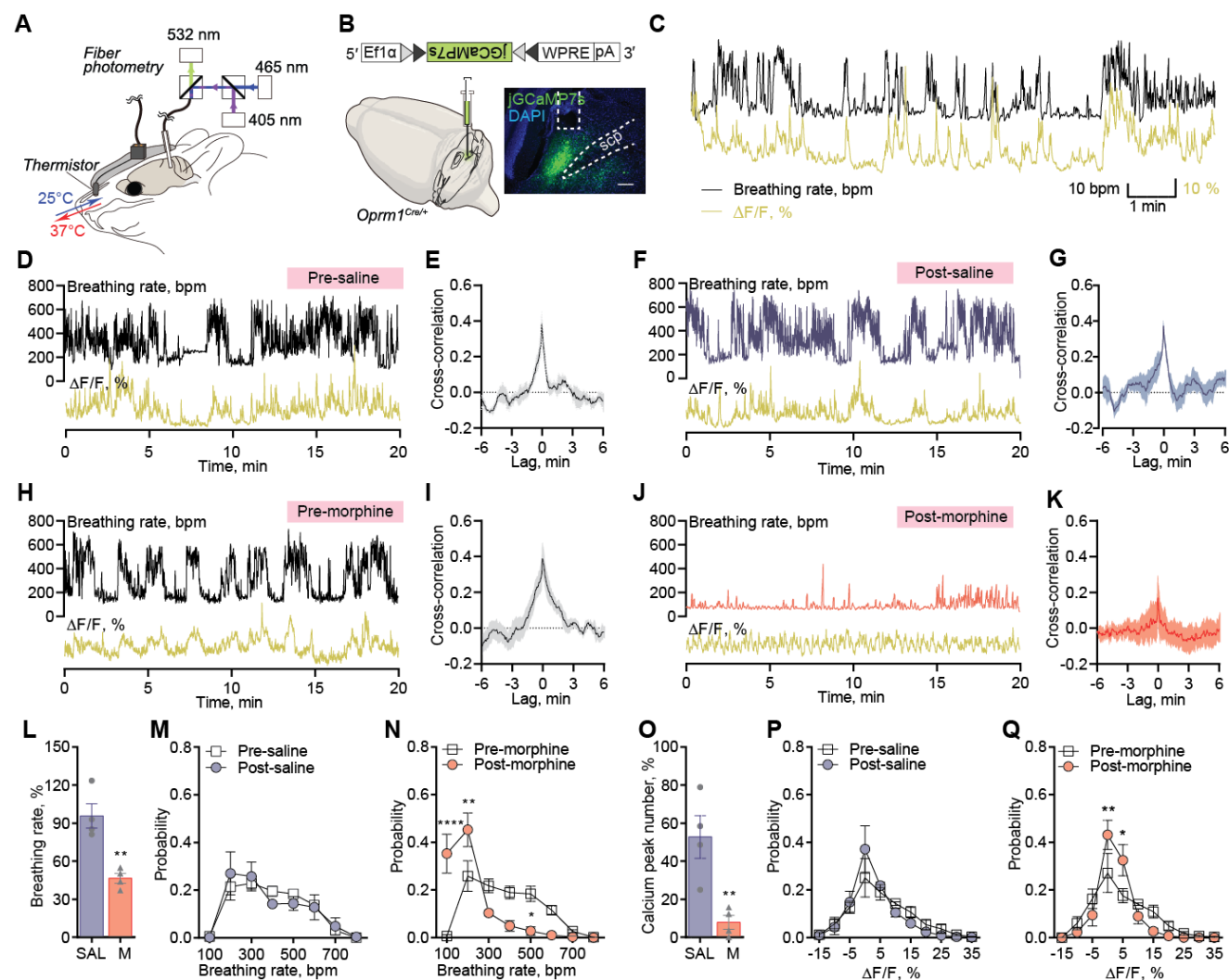
Figure 2. Morphine disrupts the tight correlation between PBL^{Oprm1} neuronal activity and respiratory rate. (**A**) Schematics of simultaneous recording of respiration and PBL^{Oprm1} calcium activity with a thermistor sensor (implanted in the nasal cavity) and fiber photometry. (**B**) The genetically encoded calcium indicator, jGCaMP7s, was specifically expressed in the PBL^{Oprm1} neurons by stereotaxic injection of AAV-DIO-jGCaMP7s into the PBL of the $Oprm1^{Cre/+}$ mice. (**C**) Time-matched traces of PBL^{Oprm1} activity and breathing rate as calculated from the thermistor sensor. (**D, F, H, J**) Simultaneously recorded PBL^{Oprm1} calcium activity and respiratory rate before and after systemic saline or morphine injection. (**E, G, I, K**) Cross-correlogram of calcium signal and respiratory rate in the pre-saline, post-saline, pre-morphine, and post-morphine groups (n = 4). (**L**) Morphine injection significantly depressed respiratory rate to around 50% of the baseline (n = 4), whereas saline injection (n = 4) did not affect the respiratory rate. (**M-N**) Normalized distribution of breathing rate before and after saline (**M**) and morphine (**N**) injections (n = 4). (**O**) The number of calcium peaks was significantly decreased after morphine injection (n = 4) compared to saline injection (n = 4). (**P-Q**) Normalized distribution of calcium signals before and after saline (**P**) and morphine (**Q**) injections (n = 4). Data are presented as mean ± SEM. Statistical tests, Unpaired t-test (**L, O**) or Two-way ANOVA with Bonferroni's multiple comparison post-hoc test (**M, N, P, Q**). *, $p < 0.05$; **, $p < 0.01$; ****, $p < 0.0001$. Scale bar, 200 μm.

421
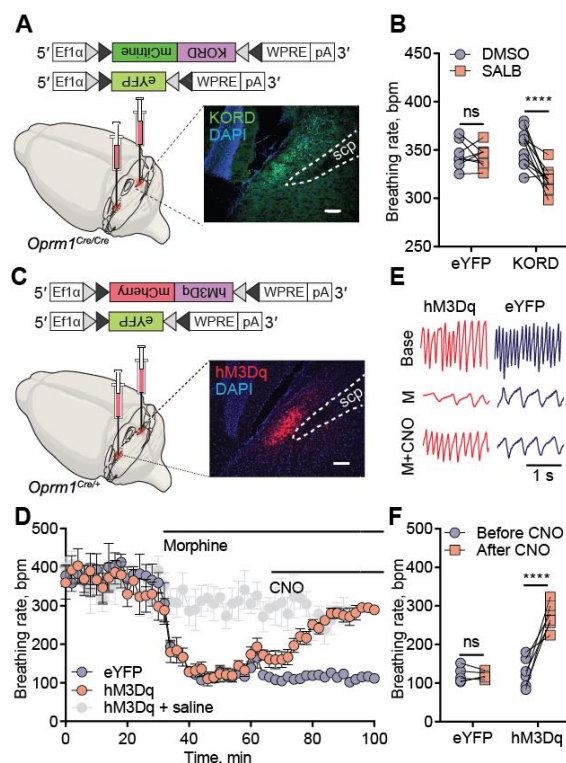
Figure 3. Inhibition of PBL^{Oprm1} neurons mimics OIRD, and chemogenetic activation of PBL^{Oprm1} neurons rescues OIRD. (**A**) Schematics of mimicking OIRD through PBL^{Oprm1} inhibition using an inhibitory κ-opioid receptor-derived DREADD (KORD). Here, AAV-DIO-KORD-mCitrine is stereotaxically injected into the bilateral PBL of *Oprm1$^{Cre/Cre}$* mice to express in the PBL^{Oprm1} neurons. (**B**) Salvinorin B (SALB, 7.5 mg/kg) injection significantly decreased respiratory rate compared to the DMSO control in the KORD-expressing mice (n = 11). In contrast, no changes were observed in eYFP-expressing mice (n = 8). (**C**) Schematics of rescuing OIRD through PBL^{Oprm1} activation by an excitatory DREADD, hM3Dq. Here, AAV-DIO-hM3Dq-mCherry was expressed in the bilateral PBL of *Oprm1$^{Cre/+}$* mice. (**D**) Activation of PBL^{Oprm1} neurons by injecting Clozapine N-oxide (CNO, 5 mg/kg) rescued the morphine-induced respiratory depression to control levels in the hM3Dq-expressing group (n = 6), but not the eYFP-expressing group (n = 5). (**E-F**) Representative plethysmograph and quantitative analysis depicting OIRD rescued by CNO injection in the hM3Dq-expressing group (n = 7), but not in the eYFP-expressing group (n = 5). Statistical tests, Two-way ANOVA with Bonferroni's multiple comparison post-hoc test. ns, not significant; ****, *p* < 0.0001. Scale bar, 200 μm.

435

436
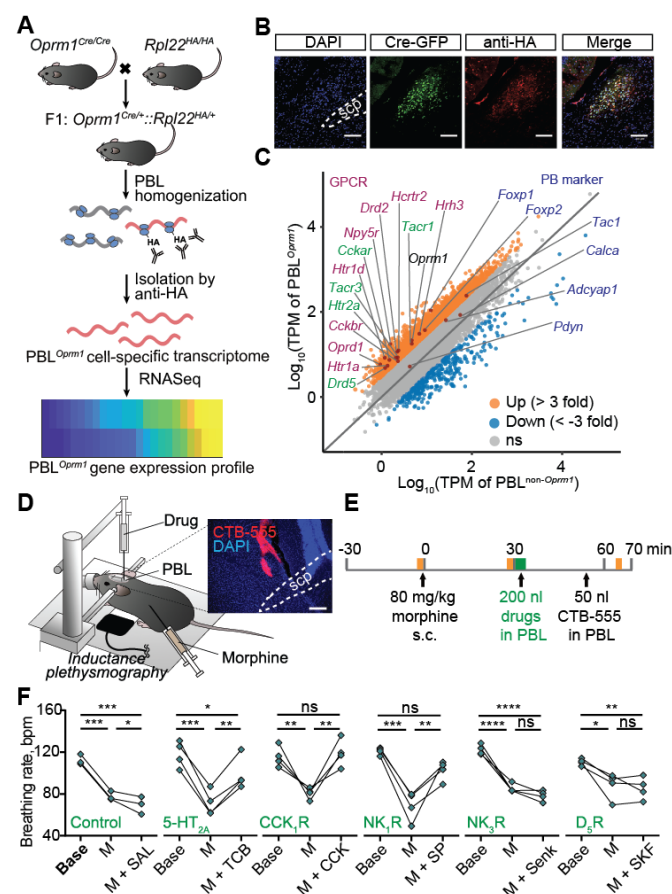
Figure 4. Rescue of OIRD through PBL^{Oprm1} stimulation via receptors identified by RiboTag RNA sequencing. (**A**) Schematics of obtaining PBL^{Oprm1} active transcriptome. *Oprm1$^{Cre/Cre}$* mice were crossed with RiboTag mice, which express hemagglutinin-tagged ribosomal protein L22 (*Rpl22^{HA}*) in a Cre-dependent manner. After collecting the PBL, active mRNAs bound to the *Rpl22^{HA}* were isolated with anti-HA antibody-mediated ribosome pull-down and sequenced. (**B**) Immunohistochemistry of the PBL region of the *Oprm1^{Cre}::Rpl22^{HA}* mice with anti-GFP and anti-HA antibodies showed that the Cre:GFP and Rpl22^{HA} were co-expressed in PBL^{Oprm1} neurons. (**C**) Fourteen GPCR mRNAs (magenta and green) were enriched more than three-fold in PBL^{Oprm1} neurons compared with non-*Oprm1* neurons in the PBL. Conventional parabrachial markers (dark blue), such as *Foxp2*, *Tac1*, and *Adcyap1* genes were enriched in PBL^{Oprm1} neurons, but not *Pdyn* and *Calca*. (**D-E**) Schematics of rescuing OIRD through artificial stimulation of receptors expressed on PBL^{Oprm1} neurons by PBL-specific injection of the agonists. Onset, histology of cholera toxin subunit B (CTB)-555 for marking the injection site. (**F**) Breathing rate decreased upon systemic morphine injection and rescued by PBL-specific injection of the agonists of 5-HT$_{2A}$, CCK$_1$R, and NK$_1$R. For the list of pharmacological agents, see Supplementary Table 1. Statistical tests, RM One-way ANOVA with Tukey's multiple comparison post-hoc test, ns, not significant; *, $p < 0.05$; **, $p < 0.01$; ***, $p < 0.001$, ****, $p < 0.0001$. Scale bar, 100 μm (**B**) or 200 μm (**D**).

452

453

454   **Supplementary Materials**

455   **Materials and Methods**

456   **Experimental Animals.** The *Oprm1$^{Cre:GFP}$* mouse line was generated from the lab of Dr. Richard Palmiter (see

457   below). C57BL/6J (Stock No. 000664), *Oprm1$^{fl/fl}$* (Stock No. 030074), RiboTag *Rpl22$^{HA/HA}$* (Stock No. 011029) and

458   Ai14 *Gt(ROSA)26Sor$^{tm14(CAG-tdTomato)Hze}$* (Stock No. 007914) mouse lines were obtained from The Jackson

459   Laboratory. Homozygous RiboTag and Ai14 mice were crossed with homozygous *Oprm1*^{Cre} mice for RiboTag and

460   anatomy experiments, respectively. Both male and female mice were used in all studies. Animals were randomized

461   to experimental groups, and no sex differences were noted. Mice were maintained on a 12-h light/dark cycle and

462   provided with food and water *ad libitum*.

463   **Generation of *Oprm1^{Cre}* mice.** A cassette encoding Cre:GFP was inserted just 5' of the initiation codon in the first

464   coding exon of the *Oprm1* gene. The 5′ arm (~3.1 kb with *Pac*I and *Sal*I sites at 5' and 3' ends, respectively) and 3′

465   arm (~4.5 kb with *Xho*I and *Not*I sites at 5' and 3' ends, respectively) of *Oprm1* gene were amplified from a

466   C57BL/6 BAC clone by PCR using Q5 Polymerase (New England Biolabs, USA) and cloned into polylinkers of a

467   targeting construct that contained mnCre:GFP, a FRT-flanked Sv40Neo gene for positive selection, and HSV

468   thymidine kinase and *Pgk*-diphtheria toxin A chain genes for negative selection. The mnCre:GFP cassette has a

469   Myc-tag and nuclear localization signals at the N-terminus of Cre recombinase, which is fused to green fluorescent

470   protein followed by a SV40 polyadenylation sequence. The construct was electroporated into G4 ES cells

471   (C57BL/6 × 129 Sv hybrid), and correct targeting was determined by Southern blot of DNA digested with *Kpn*I

472   using a ^{32}P-labeled probe downstream of the 3′ arm of the targeting construct. Twelve of the 84 clones analyzed

473   were correctly targeted. One clone that was injected into blastocysts resulted in good chimeras that transmitted the

474   targeted allele through the germline. Progeny were bred with *Gt(Rosa)26Sor-FLP* recombinase mice to remove the

475   SV-Neo gene. Mice were then continuously backcrossed to C57BL/6 mice. Routine genotyping is performed with

476   three primers: 5' CCT TCC ACT CAG AGA GTG GCG (*Oprm1* forward), 5' CCT TCC ACT CAG AGA GTG

477   GCG (*Oprm1* reverse), and 5' GGC AAA TTT TGG TGT ACG GTC AG (Cre reverse). The wild-type allele gives

478   a band of ~500 bp, while the targeted allele provides a band with ~400 bp after 34 cycles with 20-s annealing at 60

479   °C.

480   **Respiratory measurements.** *Inductance plethysmography.* Inductance plethysmography was performed by placing

481   a piezoelectric film beneath the chest of an anesthetized animal, which converts the chest movement into a voltage

482   signal. The PowerLab system with LabChart 8 software (ADInstruments Inc., USA) was used for data acquisition,

483   inspiratory and expiratory peak detection, and rate and amplitude calculation. Data were sampled at 100 or 400 Hz,

484   low-pass filtered at 10 Hz, and smoothed with a 100-ms moving window. Automatic peak detection was validated

18

485 with manual peak detection. Since the location of the sensor is subject to the slight movements of the animal's body,

486 the raw voltage value of the respiratory peak is less representative of the breathing amplitude.

487 *Whole-body plethysmography (WBP).* A custom-built WBP chamber was utilized for measuring respiratory

488 changes. The PowerLab system with LabChart 8 software was used for data acquisition, inspiratory and expiratory

489 peak detection, and rate and amplitude calculation. Data were sampled at 1 kHz, band-pass filtered at 1–10 Hz, and

490 smoothed with a 100-ms moving window. Automatic peak detection was validated with manual peak detection.

491 Mice were introduced into the WBP chamber for three 20 min habituation sessions before testing. Mice were kept

492 in the chamber for 10 - 12 min during the testing session before and after the drug injection. After 5 - 10 min of

493 chamber introduction, a stable pattern was reached, and the averaged value of a stabilized 1 min segment was

494 analyzed.

495 *Micro thermistor-based plethysmography.* A custom-built micro thermistor was implanted into the mouse nasal

496 cavity to detect changes in temperature between inspiratory and expiratory airflow (*18*). The sensor was assembled

497 using a Negative Temperature Coefficient (NTC) thermistor (TE Connectivity Ltd., Switzerland), an interconnector

498 (Mill-Max Mfg. Corp., USA), and a voltage divider (Phidgets Inc., Canada). PowerLab was used for data

499 acquisition, inspiratory and expiratory peak detection, and rate and amplitude calculation. Data were sampled at 1

500 kHz, filtered with a 0.4 - 25 Hz band-pass filter, and smoothed with a 50-ms moving window. Automatic peak

501 detection was validated with manual peak detection.

502 Minute volume is approximated by first calculating the integral of the voltage channel for each breath, summing

503 across one minute, then normalizing against the average value of the first 30 minutes. Values are shown after

504 normalization as the raw values vary considerably across animals. For comparison before and after CNO injection,

505 the averaged minute volume for 0-30 min and 30-75 min after morphine injection are used. Values during the

506 episodes when the sensor accidentally fell off due to the animal body rotation were excluded.

507 **Stereotaxic surgery.** Mice were anesthetized with isoflurane (5% induction, 1.5-2% maintenance with a nose cone;

508 Dräger Vapor 2000, Draegar, Inc., USA) and placed onto a water recirculating heating pad throughout the surgery.

509 Mice were placed on a stereotaxic frame (David Kopf Instruments, USA), the skull was exposed, and the cranium

510 was drilled with a micro motor handpiece drill (Foredom, USA: one or two holes for viral injection(s) or

511 pharmacological delivery, two holes for screws with implantation, one or two holes for optic fibers, and one hole

512 for a micro thermistor). The virus or drug was injected unilaterally (right side) or bilaterally into the PBL

513 (anteroposterior (AP), -1 mm from lambda; mediolateral (ML), ±1.5 mm; dorsoventral (DV), -3.5 mm, re-zero at

514 the midline with the same AP). Injection of the virus or drug was administered with a glass pipette (tips broken for

515 an inner diameter of 20 μm) connected to the Nanoject III Programmable Nanoliter Injector (Drummond Scientific,

516 USA) at a rate of 60 nL/min. Naloxone was injected at a rate of 100 nL/min with a syringe (65458-01, Hamilton,

19

517   USA) connected to an ultra-micropump (UMP-3, World Precision Instruments, USA). A glass pipette or syringe

518   needle was retracted from the brain slowly after 5 - 10 min. For implantation, optic fibers were implanted above the

519   injection site with the DV noted below, and the micro thermistor head was carefully lowered into the hole above

520   the nasal cavity (AP +3.5 from the nasal fissure, ML 0.3). The implants were covered with superglue and dental

521   cement for stabilization. Behavioral experiments were performed three weeks after virus injection and one week

522   after the micro-thermistor implantation unless otherwise noted.

523   For the PBL-specific conditional knockout of the *Oprm1* gene, *Oprm1$^{fl/fl}$* mice were bilaterally injected with 200 nL

524   of AAVDJ-CAG-Cre-GFP (1.25E+12 GC/mL) or control AAVDJ-CAG-GFP (2.10E+12 GC/mL) (Salk Institute

525   Viral Vector Core) into the PBL.

526   For PBL-specific rescue of the *Oprm1* gene, *Oprm1$^{Cre/Cre}$* mice were bilaterally injected with 200 nL of AAV-hSyn-

527   DIO-mCherry-T2A-FLAG-hOprm1 (1.5E+13 GC/mL) or control AAV-DIO-eYFP (2.12E+12 GC/mL) into the

528   PBL.

529   For fiber photometry, *Oprm1$^{Cre/+}$* mice were unilaterally injected with 200 nL of AAV-DIO-jGCaMP7s (3.75 E+13

530   GC/mL) or control AAV-DIO-eYFP (2.12E+12 GC/mL) into the PBL, and a stainless steel mono fiberoptic cannula

531   (400 μm diameter, 0.37 NA, Doric Lenses) was implanted 0.05 mm above the injection site.

532   For chemogenetics, 200 nL of AAV-DIO-hM3Dq-mCherry (6.56E+11 GC/mL), AAV-DIO-KORD-mCitrine, or

533   control AAV-DIO-eYFP (2.12E+12 GC/mL) was bilaterally injected into the PBL of *Oprm1$^{Cre/+}$* (for hM3Dq) or

534   *Oprm1$^{Cre/Cre}$* (for KORD) mice.

535   **Pharmacology.** Morphine sulfate (Spectrum Chemical, USA) was dissolved in 0.9% saline to make a 4 mg/mL

536   working concentration. The final concentration of morphine was 10 mg/kg in PBL-specific *Oprm1* knockout tests,

537   80 mg/kg in PBL-specific rescue of OIRD, and 40 mg/kg in all other experiments. For the characterization of

538   morphine-induced respiratory depression, mice were introduced into the WBP chamber 30 - 40 min after morphine

539   injection.

540   For PBL-specific rescue of OIRD with naloxone, wild-type mice were kept under isoflurane anesthesia until the

541   breathing rate was stable for 10 min. Then, 80 mg/kg morphine (s.c.) was systemically administered. After 30 min,

542   200 nL of 0.4 mg/mL naloxone (Somerset Therapeutics, USA) and FluoSpheres (540/560, 10% v/v, Thermo Fisher,

543   USA) mixture or a control 0.9% saline-FluoSpheres mixture was stereotaxically injected bilaterally into the PBL.

544   Breathing was analyzed from three 2-min episodes: immediately before morphine injection, 30 min after morphine

545   injection, and 10 min after naloxone or saline injection.

546   For endogenous receptor activation of PBL^{Oprm1} neurons, wild-type mice were kept under 1-1.5% isoflurane

547   anesthesia until breathing rate is stable (fluctuation < 10 bpm) for 10 min. Then, 80 mg/kg morphine (s.c.) was

20

548   systemically administered. After 30 min, 200 nL of the pharmacological agent (Supplementary Table 1) was

549   stereotaxically injected into the PBL bilaterally. 50 nL of Cholera Toxin Subunit B (CTB)-555 was subsequently

550   injected with the same coordinates to mark the injection site. Breathing was analyzed from three 2-min episodes:

551   immediately before morphine injection, 30 min after morphine injection, and 30 min after drug injection.

552   **Fiber photometry.** Fiber photometry (1-site Fiber Photometry System, 405 and 465 nm, Doric Lenses Inc, Canada)

553   with Doric Neuroscience Studio software was used to record PBL^{Oprm1} neural activities. GCaMP isosbestic

554   fluorescence (405-nm excitation) and calcium-dependent fluorescence (465-nm excitation) were recorded at a

555   sampling rate of 12 kHz, and data were analyzed with the Doric Neuroscience Studio software. F0 was calculated

556   by a least mean squares fitting of the 405-nm channel relative to the 465-nm channel, and ΔF/F was calculated as

557    $(F_{465}-F_{405\_fitted})/F_{405\_fitted}$. Data were further analyzed with custom MATLAB scripts.

558   For concurrent measurements of PBL^{Oprm1} neural activity and respiration, animals were recorded in their home cage

559   for 30 min before and 30 min after intraperitoneal (i.p.) morphine injection at 40 mg/kg. Cross-correlation analysis

560   between the calcium signals and respiration data was performed with the z-scored data, then with the MATLAB

561   "xcorr" function using the normalized option such that autocorrelations at zero lag equal 1. Calcium peaks were

562   detected with the MATLAB "findpeaks" function.

563   **Convergent cross-mapping.** State-space reconstruction models were generated using the framework of convergent

564   cross mapping (34), a nonlinear time series embedding method (53) based on the Takens theorem and its generalized

565   form (54) that builds low-dimensional manifolds from time series and makes predictions across variables. Analysis

566   and predictions were calculated using the R package rEDM 0.7.2 (https://cran.r-project.org/web/packages/rEDM/)

567   for evaluation and rEDM 0.7.4 (https://ha0ye.github.io/rEDM/) for model predictions in the RStudio environment.

568   This program was run on a dual Intel Xeon Gold 6148 Server with 384GB RAM or an Intel Core i9 2.4 GHz

569   MacBook Pro with 32 GB RAM. Key parameters were determined individually by lagged coordinate embedding

570   using the simplex function implementation in rEDM to optimize predictive skill as measured by the predicted over

571   observed rho. Parameters include the delay tau, which gives the characteristic timescale of the time series, and the

572   embedding dimensionality, which estimates the number of variables driving the system and approximates the real

573   number of variables as given by the Whitney embedding theorem (55) as minimally equal to the real number n of

574   variables, but no more than two times $n + 1$ ($n \leq E \leq 2n + 1$). The choice of tau was also informed by minimizing

575   mutual information (56). This approximately corresponds to an autocorrelation of ~0.3, which was applied if it

576   maximized predictive skill across datasets. To prevent data contamination, an exclusion radius was applied that was

577   larger than the respiration rate smoothing window of five timesteps. Whenever the data allowed, an exclusion radius

578   of E*tau was applied, unless the data was insufficient to apply this upper bound. In this case, the exclusion radius

579   would be made just larger than tau.

21

580 **Chemogenetics.** For KORD-mediated inhibition, salvinorin B (SALB, Cayman Chemical, USA) was diluted in
581 100% DMSO to make a 15 mg/mL stock solution, then further diluted in 0.9% saline (10% v/v) to make a 1.5
582 mg/mL working suspension. The control used consisted of DMSO diluted in 0.9% saline to make 10% v/v. Mice
583 were injected with 5 µL/g of body weight. The final concentration was 7.5 mg/kg. Behavioral testing was performed
584 immediately after the SALB injection. Animals that did not show the viral expression on one side were excluded
585 from the analysis.

586 For hM3Dq-mediated excitation, clozapine-N-oxide (CNO, Cayman Chemical, USA) was diluted in 0.9% saline to
587 make a 1 mg/mL working solution. Mice were injected with 5 µL/g of body weight, and the final concentration was
588 5 mg/kg. For quantification of the CNO effect, both the 0 - 10 min before and 20 - 30 min after CNO injection
589 periods were analyzed.

590 **RiboTag profiling and library generation.** Isolation of polysome-associated mRNA using RiboTag was
591 performed as previously described with minor modification (37, 57). Briefly, 250-µm thick slices containing the
592 PBL were obtained using a VT 1200S Vibratome (Leica, Germany). The region of interest was further dissected
593 with surgical scissors. Tissues were transferred into 1.5 mL microcentrifuge tubes containing homogenization buffer
594 (50 mM Tris, pH 7.5, 100 mM KCl, 12 mM $MgCl_2$, 1% Nonidet P-40, 1 mM dithiothreitol (DTT), 200 U/mL
595 RNasin, 1 mg/mL heparin, 100 µg/mL cycloheximide, and $1\times$ protease inhibitor mixture) and mechanically
596 dissociated and lysed using pellet pestles (7495211500-DS, DWK Life Sciences LLC, USA). Lysates were
597 centrifugated for 10 min at 12,000 rpm at 4 °C. Post mitochondrial supernatants were transferred to fresh 1.5 mL
598 microcentrifuge tubes. For immunoprecipitation, 4 µL of anti-hemagglutinin1.1 antibody (BioLegend, USA) was
599 added to the lysate-containing tube and incubated for 4 h at 4 °C on a microtube rotator. After incubation, magnetic
600 protein A/G beads (Cat. No. 88803; Thermo Fisher Scientific) were added to the lysate with antibody prior to
601 incubation on a microtube rotator at 4 °C overnight. The following day, the microcentrifuge tubes were placed into
602 the magnetic stand on ice. The supernatant was removed from sample tubes and used for non-Oprm1 control
603 subsequently. The magnetic beads were washed with high-salt buffer (50 mM Tris, pH 7.5, 300 mM KCl, 12 mM
604 $MgCl_2$, 1% Nonidet P-40, 1 mM DTT, and 100 µg/mL cycloheximide) to remove the non-specific binding from
605 immunoprecipitation. After washing, 350 µL of RLT plus buffer with β-mercaptoethanol from the RNeasy Mini
606 Kit (Qiagen, Germany) was added. The extraction of total RNA was performed with the RNeasy Mini Kit. All RNA
607 samples were quantified with the *Qubit RNA Assay Kit (Invitrogen, USA) and analyzed* with the RNA 6000 Pico
608 Kit (Agilent, USA).

609 Isolated RNA was prepared using the Trio RNA-Seq (Cat. No. 0507-08; NuGEN, USA). Briefly, cDNA was
610 synthesized from the total RNA using reverse transcriptase with oligo dT and resynthesized to produce double-
611 stranded cDNA. After amplification of double-stranded cDNA, cDNA was purified with AMPure XP Beads (Cat.

22

612   No. A63881; Beckman Coulter, USA), fragmented to the library, and classified using a barcoded adaptor. All

613   libraries were quantified by qPCR and analyzed *with the RNA 6000 Pico Kit.*

614   **RiboTag profiling analysis.** RNA library quality was confirmed using the 2100 Bioanalyzer (Agilent, USA).

615   Barcoded samples *were pooled* and sequenced on the NextSeq500 (Illumina, USA) with the 75-bp read length

616   single-end format. Image analysis and base calling were conducted using the Illumina CASAVA-1.8.2 software.

617   Sequencing read quality was evaluated with the FastQC package

618   (http://www.bioinformatics.babraham.ac.uk/projects/fastqc). Fastq reads were aligned to the reference genome

619   (GRCm38.p6) using the STAR tool (version 2.7.2) (58). The quantification package RSEM (version 1.2.28) (59)

620   was utilized to calculate gene expression from BAM files. In doing so, estimated count and TPM (Transcripts Per

621   Million) were computed. Fold changes were calculated from TPM values (estimated counts > 20) between HA-tag

622   and controls. To visualize fold changes, we utilized the ggplot2 package from R. UP (> 3 fold change) and DOWN

623   (< -3 fold change) were highlighted with orange and blue colors, respectively. Key genes for the parabrachial marker

624   and GPCRs were further annotated.

625   **Histology.** Mice were euthanized with CO_2 at a flow rate of 1.2 liters per minute (LPM), perfused intracardially

626   with ice-cold phosphate-buffered saline (PBS), and fixed with 4 % paraformaldehyde (PFA) in phosphate buffer

627   (PB). The brain was extracted, post-fixed in 4 % PFA overnight and dehydrated in 30 % sucrose in PBS until sliced.

628   Frozen brains were cut into 50 µm coronal slices using a CM 1950 cryostat (Leica, Germany) and stored in PBS

629   before mounting. The slices were mounted on Superfrost Microscope Slides (Fisher Scientific, USA) with DAPI

630   Fluoromount-G mounting media (Southern Biotech, USA) for imaging.

631   **Immunohistochemistry.** To validate the co-expression of Cre:GFP and Rpl22:HA in PBL^{Oprm1} neurons,

632   immunohistochemistry for HA and GFP was performed. To validate the conditional knockout of the *Oprm1* gene

633   in the PBL, we performed immunohistochemistry for MOR.

634   Mice were euthanized with CO_2 at a flow rate of 1.2 LPM, perfused intracardially with ice-cold PBS, and fixed

635   with 4 % PFA in PB. The brain was extracted, post-fixed in 4 % PFA overnight and dehydrated in 30 % sucrose in

636   PBS until sliced. Frozen brains were cut into 30 µm coronal slices with a CM 1950 cryostat and stored in PBS.

637   Sections were washed with PBST (PBS with 3% Tween-20, Fisher BioReagents, USA). After blocking with 3 %

638   normal donkey serum (NDS, Jackson ImmunoResearch Inc., USA) for 1 h at room temperature and rinsing with

639   PBST, the slices were incubated with the corresponding antibodies: mouse monoclonal anti-HA1.1 (1:1000,

640   BioLegend, USA), chicken anti-GFP (1:1000, Aves Labs Inc, USA), and rabbit anti-MOR (1:1000, ImmunoStar,

641   USA) antibodies at 4 °C for overnight (anti-HA1.1 and anti-GFP) or 24 h (anti-MOR). The next day, brain tissues

642   were rinsed with PBST and incubated in Alexa Fluor® 647-conjugated Donkey Anti-Mouse IgG, Alexa Fluor® 488-

643   conjugated Donkey Anti-Chicken IgY, and Alexa Fluor® 647-conjugated Donkey Anti-Rabbit IgG (1:1000, Jackson

644   ImmunoResearch Inc., USA) in 3 % NDS for 90 min at room temperature. After washing with PBS, brain slices

645   were mounted on Superfrost Microscope Slides with DAPI Fluoromount-G mounting media for imaging.

646   **RNA *in situ* hybridization.** RNA *in situ* hybridization was performed using the RNAscope Fluorescent Multiplex

647   Assay using the probes and kits purchased from Advanced Cell Diagnostics (ACD, USA). Brains were collected

648   from wild type mice and immediately frozen with 2-methylbutane chilled with dry ice. Frozen brains were cut into

649   20-µm coronal slices with a CM 1950 cryostat and directly mounted onto the Superfrost Plus Microscope Slides

650   (Fisher Scientific). Sample preparation, pretreatment, and signal detection were performed according to the ACD

651   protocols. Probes used are listed below: *Oprm1* (ACD #315841), *Htr2a* (#401291), *Cckar* (#313751), *Drd5*

652   (#494411), *Tacr3* (#481671), *Tacr1* (#428781), *Cre* (#402551), *Slc17a6* (#319171), and *Slc32a1* (#319191).

653   Two to three representative images from the PBL (AP = -5.0 to -5.2) were selected from n = 3 mice, and PBL cells

654   within a field of view of 300 µm x 300 µm (for *Oprm1* colocalization with *Cre*, *Htr2a*, *Cckar*, *Tacr3*, *Tacr1*, and

655   *Drd5*) or 600 µm x 600 µm (for *Oprm1* colocalization with *Slc17a6* and *Slc32a1*) were used for quantification.

656   Quantification of the colocalization is done manually with ImageJ software according to the ACDBio technical

657   note. DAPI-stained nuclei were first identified, then the cell contour was defined with a 2-µm radius surrounding

658   the DAPI signals. Cells containing at least five puncta inside the imaginary boundary were labeled as positive.

659   **Imaging.** Images for verification of injection and implantation site and anti-MOR staining for conditional knockout

660   validation were taken with a BZ-X710 all-in-one fluorescence microscope with BZ-X viewer software under a 10X,

661   0.45 NA objective (Keyence, Japan). Images for anti-HA & anti-GFP immunostaining, RNAscope, and

662   *Oprm1^{Cre}*::Ai14 expression characterization were acquired with an FV3000 Confocal Laser Scanning Microscope

663   with FV31S-SW software under a 20X, 0.75 NA or 40X, 0.95 NA UPLSAPO objective (Olympus, Japan). For

664   comparison, images were processed with the same gain, offset, and exposure time.

665   **Statistical Analysis.** All data are shown as mean ± SEM and analyzed using either a student's t-test, one-way

666   ANOVA with Tukey's *post hoc* comparison, or two-way ANOVA with Bonferroni's *post hoc* comparison. All

667   statistical analyses were performed with Prism 6 (GraphPad Software Inc., USA). ns $p > 0.05$, * $p < 0.05$, ** $p <$

668   0.01, *** $p < 0.001$, **** $p < 0.0001$.

669   For a detailed list of resources, please refer to Supplementary Table 2.

24

670   **Supplementary Figures**

671
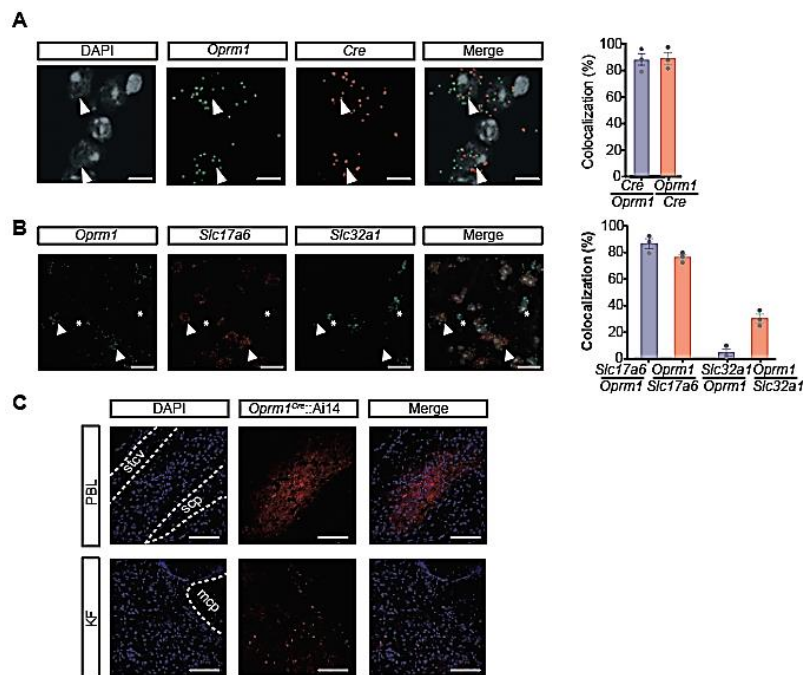
672   **Supplementary Figure 1.** Characterization of the *Oprm1^{Cre}* mouse line and PBL^{Oprm1} neurons. (**A**) RNA *in situ*
673   hybridization and quantification of the colocalization for *Oprm1* and *Cre* mRNAs in the PBL of *Oprm1$^{Cre/+}$* mice
674   (n = 902 cells from 3 animals). Arrowheads, double-labeled cells. Scale bar, 10 μm. (**B**) RNA *in situ* hybridization
675   and quantification of the colocalization for *Oprm1*, *Slc17a6* (encoding VGLUT2), and *Slc32a1* (encoding VGAT)
676   mRNAs in the PBL of wild type mice (n = 1552 and 1431 cells from 3 animals). Arrowheads, *Oprm1$^+$ / Slc17a6$^+$*
677   cells; asterisks, *Oprm1$^-$ / Slc32a1$^+$* cells. Scale bar, 50 μm. (**C**) Example histology from *Oprm1^{Cre}::*Ai14 double
678   transgenic mice showing tdTomato expression in the PBL and KF under the same microscope settings. Anatomical
679   landmarks for PBL: stcv, ventral spinocerebellar tract; scp, superior cerebellar peduncle; mcp, middle cerebellar
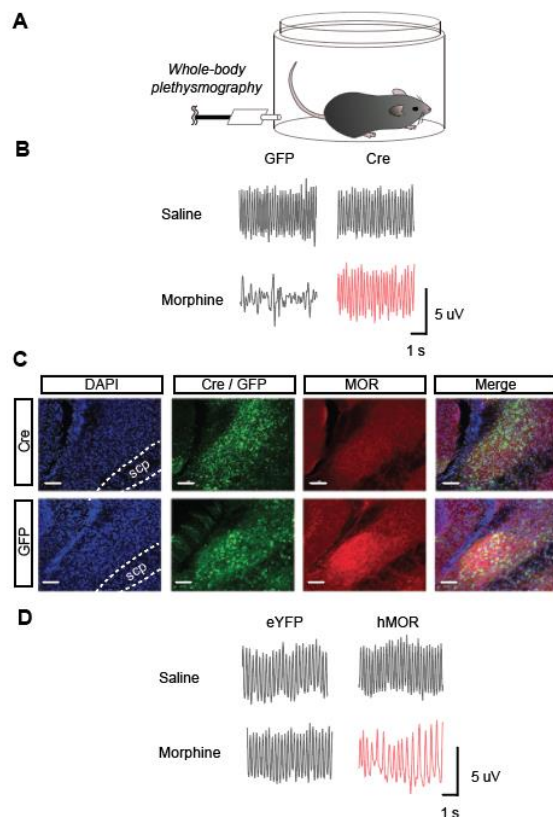680   peduncle. Scale bar, 200 μm.

681

Supplementary Figure 2. MOR signaling in the PBL is indispensable for OIRD. (**A**) Whole-body plethysmography measured respiratory parameters before and after systemic injection of saline and morphine, after conditional ablation (**B**) and rescue (**D**) of the MOR signaling in the PBL. (**B**) Example plethysmograph after saline and morphine injections into the *Oprm1$^{fl/fl}$* mice expressing AAV-GFP and AAV-Cre-GFP in the PBL. (**C**) Confirmation of MOR deletion by MOR immunohistochemistry after stereotaxic injection of AAV-Cre-GFP and control AAV-GFP into the PBL of the *Oprm1$^{fl/fl}$* mice. Scale bar, 100 μm. (**D**) Example plethysmograph after saline and morphine injections into the *Oprm1$^{Cre/Cre}$* mice expressing AAV-DIO-eYFP and AAV-DIO-hMOR in the PBL.

689

26
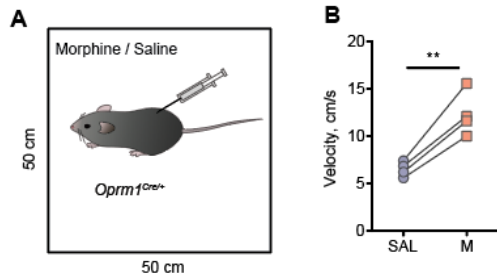
Supplementary Figure 3. Morphine effect on locomotor sensitization. (**A**) Locomotor activity of $Oprm1^{Cre/+}$ mice after morphine (40 mg/kg, i.p.) or saline injection was measured in the open field. (**B**) Systemic morphine injection increased locomotor activity in $Oprm1^{Cre/+}$ mice. Paired t-test, **, $p < 0.01$.

27

699
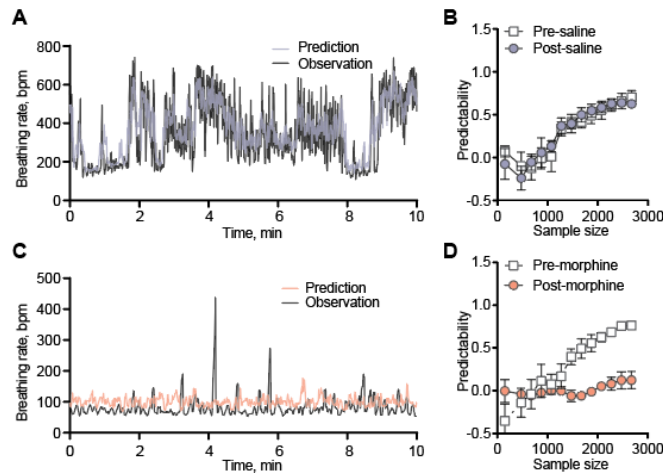
Supplementary Figure 4. Morphine eliminated the breathing predictor. Convergent cross-mapping (CCM) prediction of breathing rate using calcium activity as inputs before and after saline (0.9%, i.p., **A** and **B**) and morphine (40 mg/kg, i.p., **C** and **D**) injection. (**A**) After saline injection, the predicted and observed breathing rate traces followed closely with each other during the 10-min example. (**B**) Model predictability increased with the sample size before and after saline injection (n = 4). (**C**) After morphine injection, the predicted and observed breathing rate traces no longer matched with each other. (**D**) Model predictability increased with the sample size before morphine injection, but the relationship was completely abolished after morphine injection (n = 4).

707

708
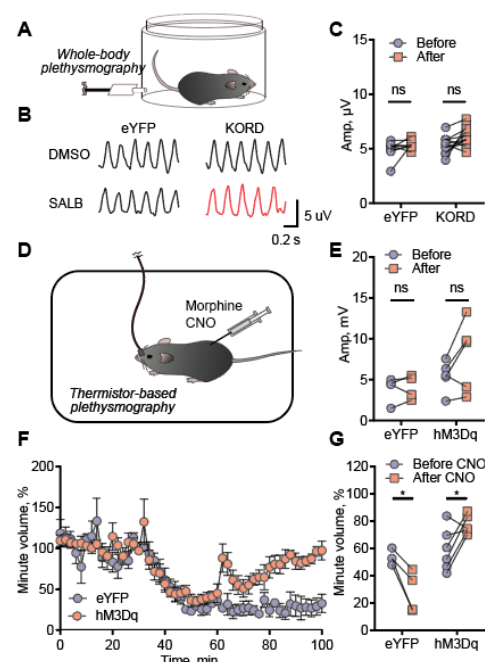
Supplementary Figure 5. (**A**) Whole-body plethysmography was used to measure respiratory parameters before and after systemic injection of DMSO and SALB in the *Oprm1*$^{Cre/Cre}$ mice expressing AAV-DIO-eYFP and AAV-DIO-KORD in PBL^{Oprm1} neurons. (**B**) Example plethysmograph after DMSO and 7.5 mg/kg SALB injections in eYFP and KORD groups. KORD-expressing animals displayed a slower respiratory rate after SALB injection compared to other groups. (**C**) Respiratory amplitude was not significantly changed before and after SALB injection, in both eYFP (n = 8) and KORD (n = 11)-expressing animals. Two-way ANOVA with Bonferroni's multiple comparison post-hoc test, ns, not significant. (**D**) Thermistor-based plethysmography was used for measuring respiration before and after systemic injection of 40 mg/kg morphine and CNO in the *Oprm1*$^{Cre/+}$ mice expressing AAV-DIO-eYFP and AAV-DIO-hM3Dq in PBL^{Oprm1} neurons. (**E**) Respiratory amplitude was not significantly changed before and after CNO injection, in both eYFP (n = 5) and hM3Dq-expressing animals (n = 6). Although there was a trend of increase in the hM3Dq group, it failed to reach statistical significance. Two-way ANOVA with Bonferroni's multiple comparison post-hoc tests, ns, not significant. (**F**) Activation of PBL^{Oprm1} neurons by injecting CNO (5 mg/kg, i.p.) in the hM3Dq-expressing group (n = 6) completely rescued the minute volume to baseline level after morphine-induced respiratory depression, but not in eYFP-expressing group (n = 5). (**G**) Quantitative analysis of **F** showing CNO injection significantly increased the minute volume in the hM3Dq-expressing group (n = 6), whereas failed to rescue in the eYFP-expressing group (n = 5). Two-way ANOVA with Bonferroni's multiple comparison post-hoc test. *, $p < 0.05$.

29

726
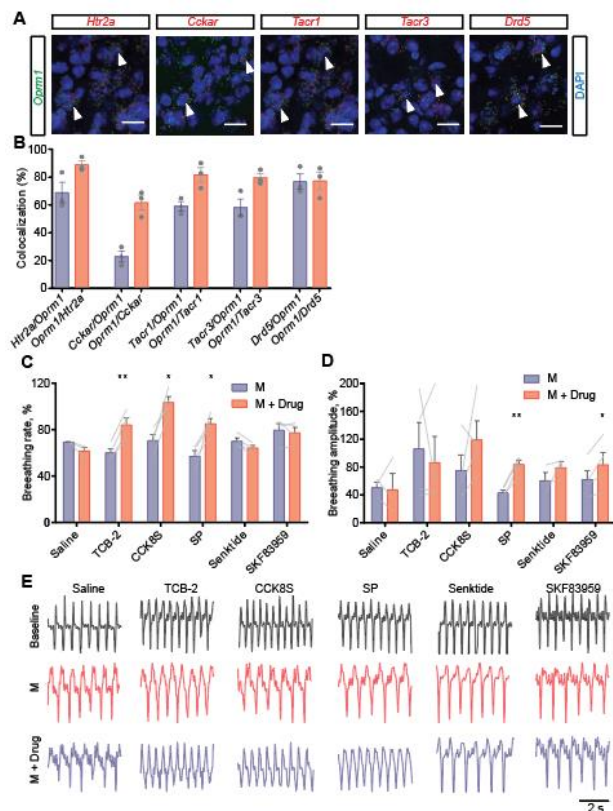
Supplementary Figure 6. Rescuing of OIRD by activating endogenous GPCRs expressed on PBL^{Oprm1} neurons. (**A**) RNA *in situ* hybridization confirms the co-expression of mRNA of *Oprm1* and five selected GPCRs, *Htr2a*, *Cckar*, *Tacr1*, *Tacr3*, and *Drd5*, in the wild type mice. Arrowheads, double-labeled cells. Scale bar, 50 μm. (**B**) Quantification of RNA *in situ* hybridization showing the colocalization of *Oprm1* and selective GPCR genes in the PBL of wild type mice (770, 539, 836, 657, 431 cells for *Htr2a*, *Cckar*, *Tacr1*, *Tacr3*, and *Drd5*, respectively). (**C-D**) Normalized breathing rate (**C**) and amplitude (**D**) before morphine injection (Baseline), 30 minutes after morphine injection (80 mg/kg, s.c., M), and 30 minutes after drug injection into the PBL (M + Drug), for all six drugs tested. Large variations in amplitude are due to the technical limitations of the piezoelectric sensor since its location is subjective to the slight movements of the animal's body. Paired t-test, *, $p < 0.05$; **, $p < 0.01$. **e** Example plethysmograph showing the breathing rhythm changes at each stage of the experiment. Note the decreased breathing rate after morphine injection and increased breathing rate after TCB-2, CCK8S, and SP injections. The exact shape of the plethysmograph varies due to the placement of the piezoelectric sensor.

739

30

740
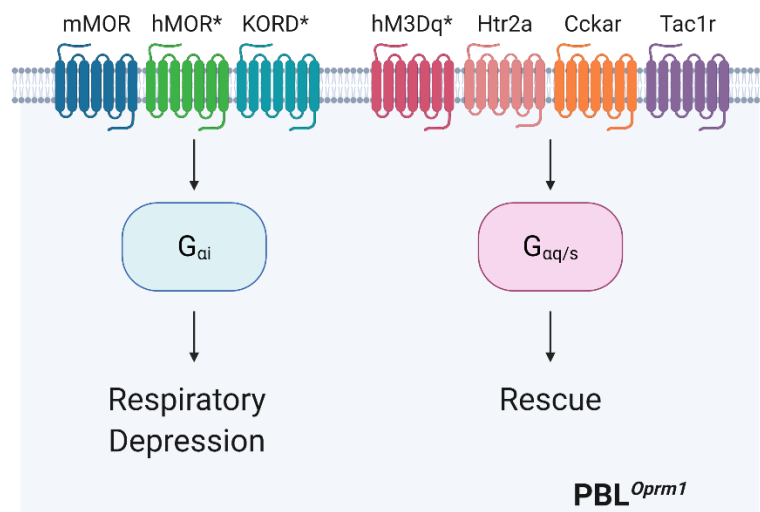
Supplementary Figure 7. Summary of the current study. PBL^{Oprm1} neurons are critical players in OIRD pathogenesis and promising therapeutic targets for treating OIRD. In intact mice, inhibition of PBL^{Oprm1} neurons through G_i-coupled GPCRs via endogenous MOR (mMOR), human MOR (hMOR), and KOR-derived DREADD (KORD) leads to respiratory depression. In contrast, activation of these neurons via artificial (hM3Dq) or endogenous $G_{q/s}$-coupled GPCRs (Htr2a, Cckar, Tac1r) rescues OIRD. Artificial GPCRs are marked with asterisks. Created with BioRender.com.

747

748

749

750

751

752

753

754

755

756

757 **Supplementary Table 1. List of pharmacological agents used in the current study.**

Drug Name	Receptor (Gene)	Receptor Family	Concentration	Solvent	Company
Naloxone	MOR (*Oprm1*)	Gi	0.4 mg/mL (i.c., intracranial)	0.9% saline	Somerset Therapeutics
Morphine	MOR (*Oprm1*)	Gi	80 mg/kg (s.c., for anesthesia experiments); 10 mg/kg (i.p., for PBL-specific *Oprm1* knockout); 40 mg/kg (i.p., for all other experiments)	0.9% saline	Spectrum Chemical
Salvinorin B (SALB)	KORD	Gi	7.5 mg/kg (i.p.)	0.9% saline containing 10% DMSO	Cayman Chemical
Clozapine-N-oxide (CNO)	hM3Dq	Gq	5 mg/kg (i.p.)	0.9% saline	Cayman Chemical
TCB-2	5-HT$_{2A}$ (*Htr2a*)	Gq	1 mg/mL (i.c.)	0.9% saline	Tocris Bioscience
CCK Octapeptide, sulfated (CCK8S)	CCK$_1$R (*Cckar*)	Gq	1 mg/mL (i.c.)	0.9% saline	Abcam
Substance P	NK$_1$R (*Tacr1*)	Gq, Gs	1 mg/mL (i.c.)	0.9% saline	Cayman Chemical
Senktide	NK$_3$R (*Tacr3*)	Gq	1 mg/mL (i.c.)	0.9% saline	Cayman Chemical
SKF-83959	D$_5$R (*Drd5*)	Gs	1 mg/mL (i.c.)	0.9% saline containing 5% DMSO	Tocris Bioscience

758

759 **Supplementary Table 2. Key Resources Table**

Type	Designation	Source or reference	Identifiers
Mouse strains	Oprm1-Cre:GFP	Laboratory of Dr. Richard Palmiter	N/A
	Wild type C57BL/6J	Jackson Laboratory	Stock No. 000664
	RiboTag *Rpl22$^{HA/HA}$*	Jackson Laboratory	Stock No. 011029
	Ai14 *Gt(ROSA)26Sor$^{tm14(CAG-tdTomato)Hze}$*	Jackson Laboratory	Stock No. 007914
Virus	AAVDJ-CAG-Cre-GFP	Salk Institute Viral Vector Core	N/A
	AAVDJ-CAG-GFP	Salk Institute Viral Vector Core	N/A
	AAV-hSyn-DIO-mCherry-T2A-FLAG-hOprm1	Laboratory of Dr. Matthew Banghart	N/A
	AAV1-syn-FLEX-jGCaMP7s-WPRE	Addgene	Addgene# 104491
	AAVDJ-EF1a-DIO-hM3D(Gq)-mCherry	Salk Institute Viral Vector Core	Addgene# 50460
	AAV-DIO-KORD-mCitrine	Laboratory of Dr. Richard Palmiter	N/A
	AAV1-DIO-eYFP	Laboratory of Dr. Richard Palmiter	N/A
Antibodies	Anti-hemagglutinin1.1, mouse (1:1000)	BioLegend	RRID AB_2565335
	Anti-GFP, chicken (1:1000)	Aves Labs	RRID AB_2307313
	Anti-MOR, rabbit (1:1000)	ImmunoStar	RRID AB_572251
	Alexa Fluor® 647-conjugated Donkey Anti-Mouse IgG (1:1000)	Jackson ImmunoResearch Laboratories	RRID AB_2340863
	Alexa Fluor® 488-conjugated Donkey Anti-Chicken IgY (1:1000)	Jackson ImmunoResearch Laboratories	RRID AB_2340375
	Alexa Fluor® 647-conjugated Donkey Anti-Rabbit IgG (1:1000)	Jackson ImmunoResearch Laboratories	RRID AB_2492288
RNAscope probes	Oprm1	Advanced Cell Diagnostics	315841
	Htr2a	Advanced Cell Diagnostics	401291
	Cckar	Advanced Cell Diagnostics	313751
	Drd5	Advanced Cell Diagnostics	494411

	Tacr3	Advanced Cell Diagnostics	481671
	Tacr1	Advanced Cell Diagnostics	428781
	Cre	Advanced Cell Diagnostics	402551
	Slc17a6	Advanced Cell Diagnostics	319171
	Slc32a1	Advanced Cell Diagnostics	319191
Chemicals	FluoSpheres 540/560 (10% v/v)	Thermo Fisher	Cat# F8809
	Cholera Toxin Subunit B-555	Invitrogen	Cat# C34776
	Naloxone	Somerset Therapeutics	Cat# 70069007110
	Morphine	Spectrum Chemical	Cat# M1167
	TCB-2	Tocris Bioscience	Cat# 2592
	CCK Octapeptide, sulfated	Abcam	Cat# ab120209
	Substance P	Cayman Chemical	Cat# 24035
	Senktide	Cayman Chemical	Cat# 16721
	SKF-83959	Tocris Bioscience	Cat# 2074
	Clozapine N-oxide	Cayman Chemical	Cat# 16882
	Salvinorin B	Cayman Chemical	Cat# 11488
	2-methylbutane	Fisher Chemical	Cat# O35514
Software	Doric Neuroscience Studio	Doric Lenses	N/A
	RStudio	RStudio	Version 1.2.5001
	rEDM	https://cran.r-project.org/web/packages/rEDM/	Version 0.7.2
	rEDM	https://ha0ye.github.io/rEDM/	Version 0.7.4
	LabChart	ADInstruments	Version 8
	BZ-X viewer	Keyence	N/A
	OlyVIA	Olympus Life Science	N/A
	PRISM	GraphPad Software	Version 6
	Illustrator	Adobe	Version CS6 and CC2018

760